



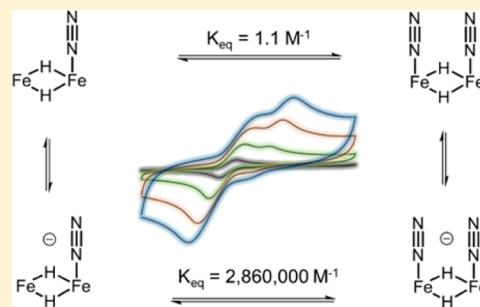
# A $10^6$ -Fold Enhancement in $\text{N}_2$ -Binding Affinity of an $\text{Fe}_2(\mu\text{-H})_2$ Core upon Reduction to a Mixed-Valence $\text{Fe}^{\text{II}}\text{Fe}^{\text{I}}$ State

Jonathan Rittle, Charles C. L. McCrory, and Jonas C. Peters\*

Division of Chemistry and Chemical Engineering, California Institute of Technology, 1200 East California Boulevard, Pasadena, California 91125, United States

## Supporting Information

**ABSTRACT:** Transient hydride ligands bridging two or more iron centers purportedly accumulate on the iron–molybdenum cofactor (FeMoco) of nitrogenase, and their role in the reduction of  $\text{N}_2$  to  $\text{NH}_3$  is unknown. One role of these ligands may be to facilitate  $\text{N}_2$  coordination at an iron site of FeMoco. Herein, we consider this hypothesis and describe the preparation of a series of diiron complexes supported by two bridging hydride ligands. These compounds bind either one or two molecules of  $\text{N}_2$  depending on the redox state of the  $\text{Fe}_2(\mu\text{-H})_2$  unit. An unusual example of a mixed-valent  $\text{Fe}^{\text{II}}(\mu\text{-H})_2\text{Fe}^{\text{I}}$  is described that displays a  $10^6$ -fold enhancement of  $\text{N}_2$  binding affinity over its oxidized congener, quantified by spectroscopic and electrochemical techniques. Furthermore, these compounds show promise as functional models of nitrogenase as substantial amounts of  $\text{NH}_3$  are produced upon exposure to proton and electron equivalents. The  $\text{Fe}(\mu\text{-H})\text{Fe}(\text{N}_2)$  sub-structure featured herein was previously unknown. This subunit may be relevant to consider in nitrogenases during turnover.



The intimate mechanism of biological nitrogen fixation at the FeMo-cofactor (FeMoco) of nitrogenase enzymes is a fascinating, unsolved problem. One or two of the central iron atoms of the FeMoco have been highlighted as plausible  $\text{N}_2$  binding sites.<sup>1</sup> Yet, despite a supporting body of biochemical and spectroscopic data,<sup>2,3</sup> in addition to synthetic  $\text{Fe}-\text{N}_2$  model chemistry establishing that  $\text{N}_2$  reduction to  $\text{NH}_3$  is possible at an iron center,<sup>4–6</sup> there remains the question as to how an iron site (or sites) that resides within a sulfide-rich environment would facilitate  $\text{N}_2$  binding. To date, there is little synthetic precedent for  $\text{Fe}-\text{N}_2$  complexes that feature sulfur within the immediate iron coordination sphere,<sup>7,8</sup> and there are no synthetic  $\text{Fe}-\text{N}_2$  species where only sulfur ligates the iron center.

An interesting possibility to consider is whether iron hydrides, either terminal or bridging, might facilitate better  $\text{N}_2$  binding at an iron site of FeMoco by increasing its  $\pi$ -basicity, owing to the relatively strong ligand field exerted by a hydride.<sup>9</sup> Hydride ligands could be installed under the electron-loading phase, prior to  $\text{N}_2$  uptake, a phase that is presumably leveled by the concomitant delivery of protons to iron and/or sulfur sites. It is noteworthy in this context that a bridging hydride form of the FeMoco (i.e.,  $\text{Fe}(\mu\text{-H})\text{Fe}$ ) has been proposed based on spectroscopic data under turnover conditions.<sup>10</sup> While elimination of  $\text{H}_2$  upon  $\text{N}_2$  binding has been suggested as a way to rationalize presumed obligatory  $\text{H}_2$  elimination during  $\text{N}_2$  reduction to two equiv  $\text{NH}_3$ ,<sup>11,12</sup> an additional possibility to consider is that cofactor bound hydrides afford a sufficiently covalent  $\text{Fe}-\text{N}_2$  interaction to render  $\text{N}_2$  binding and reduction at an iron site (or sites) favorable.

Because bridging rather than terminal hydrides have been implicated as observable intermediates, we sought to prepare  $\text{Fe}(\mu\text{-H})\text{Fe}$  model complexes that have an affinity for  $\text{N}_2$ . Terminal  $\text{Fe}-\text{H}$  complexes are now well established to bind  $\text{N}_2$ ,<sup>13,14</sup> even with sulfur in the immediate iron coordination sphere,<sup>7</sup> but to our knowledge there are no synthetic  $\text{Fe}-\text{N}_2$  complexes featuring hydrides bridging another Fe center. This situation exists despite the fact that there are hundreds of crystallographically characterized complexes featuring bridging hydride  $\text{Fe}(\mu\text{-H})\text{Fe}$  subunits.<sup>15</sup>

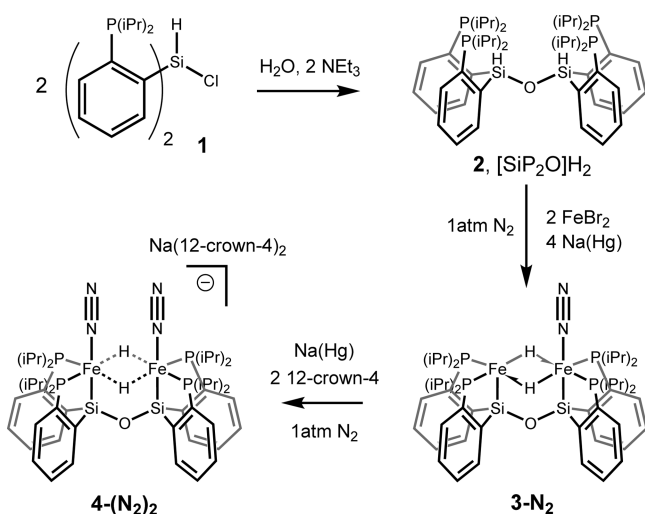
Herein we present a new binucleating scaffold that accommodates two bridging hydrides to afford a  $\text{Fe}(\mu\text{-H})_2\text{Fe}$  subunit. This structural motif is shown to be compatible with  $\text{N}_2$  binding and reductive protonation to release a substoichiometric but nevertheless substantial amount of  $\text{NH}_3$ . In addition, reversible coordination of  $\text{N}_2$  to the second iron site is observed, and the  $\text{N}_2$  binding affinity is shown to increase by 6 orders of magnitude upon further reduction of the  $\text{N}_2\text{-Fe}(\mu\text{-H})_2\text{Fe}$  subunit by one electron (Scheme 1). The  $S = 1/2$  form,  $\{\text{N}_2\text{-Fe}(\mu\text{-H})_2\text{Fe}-\text{N}_2\}^+$ , shows strong hyperfine coupling through the bridging hydride ligands.

## RESULTS

**Synthesis and Structure of  $3\text{-N}_2$ .** To support an unsaturated  $\text{Fe}(\mu\text{-H})\text{Fe}$  unit, we synthesized the bulky hexadentate ligand,  $[\text{SiP}_2\text{O}]\text{H}_2$  (**2**). Compound **2** is synthesized by the controlled hydrolysis of previously reported bis(o-

Received: July 21, 2014

Published: September 3, 2014

Scheme 1. Synthesis of  $[\text{SiP}_2\text{O}]_2\text{H}_2$  and Supported Di-iron Complexes

diisopropylphosphino-phenyl)-chlorosilane (**1**) (Scheme 1).<sup>7</sup> The ligand exhibits a singlet in the  $^{31}\text{P}\{^1\text{H}\}$  NMR spectrum ( $\delta = -0.5$  ppm) and a triplet in the  $^{29}\text{Si}\{^1\text{H}\}$  spectrum ( $\delta = -30.4$  ppm,  $J_{\text{Si-P}} = 27$  Hz). Two Si-H vibrations are observed in the solid state ( $2199$  and  $2166\text{ cm}^{-1}$ , KBr).

Complexation of  $[\text{SiP}_2\text{O}]_2\text{H}_2$  with two equivalents of  $\text{FeBr}_2$ , followed by reduction with  $\text{Na(Hg)}$  under  $1\text{ atm}$  of  $\text{N}_2$  (Scheme 1), furnishes **3-N<sub>2</sub>** in 60% yields on gram scales.  $^{57}\text{Fe}$ -enriched **3-N<sub>2</sub>** can be obtained by substituting one equivalent of  $\text{FeBr}_2$  with  $^{57}\text{FeCl}_2$  (44% yield). The solid-state structure of **3-N<sub>2</sub>** is shown in Figure 1 and confirms the presence of two Fe atoms supported by the ligand framework. Two bridging hydride ligands, presumably arising from in situ activation of the Si-H units in **2**, are located in the Fourier difference map ca.  $1.64\text{ \AA}$  from Fe2 and ca.  $1.69\text{ \AA}$  from Fe1. The long  $\text{H50}\cdots\text{H51}$  distance ( $2.21(2)\text{ \AA}$ ) confirms their assignment as hydrides and not a stretched-dihydrogen ligand. Furthermore, no interaction is observed between the Si and H atoms as reflected by long  $\text{H}\cdots\text{Si}$  distances ( $3.08(2)$  to  $2.53(2)\text{ \AA}$ ).  $\text{N}_2$  coordinates selectively to Fe2 in a terminal fashion with an  $\text{Fe2-N1}$  distance of  $1.8474(9)\text{ \AA}$  and an  $\text{N1-N2}$  distance of  $1.114(1)\text{ \AA}$ , reflecting a minimal degree of activation (the N-N distance in free  $\text{N}_2$  is  $1.0976\text{ \AA}$ ). The shortest methyl group Fe-C distance is  $3.719(1)\text{ \AA}$  (to Fe1), ruling out the presence of agostic interactions in the solid state. While the Fe-P distances are similar for both sites, the Fe1-Si1 bond distance ( $2.1644(4)\text{ \AA}$ ) is markedly shorter than that of Fe2-Si2 ( $2.2594(4)\text{ \AA}$ ).

The structure of **3-N<sub>2</sub>** is maintained in solution in the absence of additional  $\text{N}_2$ . The room temperature  $^1\text{H}$  NMR spectrum of **3-N<sub>2</sub>** is unchanged following multiple freeze-pump-thaw cycles, indicating that the  $\text{N}_2$  ligand is not labile. NMR spectra collected on **3-N<sub>2</sub>** indicate an asymmetric molecule at low temperatures (Figure 2). Four resonances are observed in the  $^{31}\text{P}$  NMR spectrum of **3-N<sub>2</sub>** at  $213\text{ K}$  (Supporting Information), and the hydride ligands are nonequivalent at temperatures below  $273\text{ K}$  (vide infra).<sup>16</sup> The observed asymmetry can be explained in part by exclusive  $\text{N}_2$  coordination to one Fe site.<sup>17</sup>

At  $373\text{ K}$ , the Fe sites were found to be equivalent on the NMR time scale. Eleven resonances are observed in the  $^1\text{H}$  NMR spectrum (toluene- $d_8$ ,  $1\text{ atm Ar}$ ), including a single

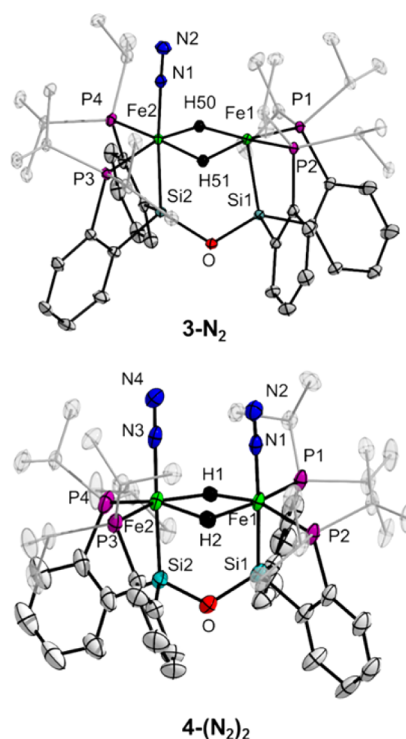


**Figure 1.** X-ray diffraction crystal structures of **3-N<sub>2</sub>** and **4-(N<sub>2</sub>)<sub>2</sub>** with thermal ellipsoids drawn at 50% probability. Hydrogen atoms (other than the iron hydrides), the  $\text{Na(12-crown-4)}_2$  cation of **4-(N<sub>2</sub>)<sub>2</sub>**, and cocrystallized solvent molecules have been removed for clarity. The isopropyl substituents have been rendered transparent to aid in visualization of the inner coordination sphere around the diiron unit.

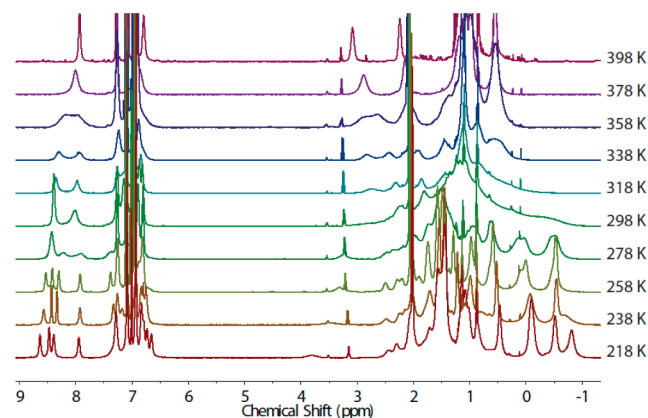


**Figure 2.** Variable temperature  $500\text{ MHz } ^1\text{H}$  NMR spectra of **3-N<sub>2</sub>** in toluene- $d_8$ . To exclude additional  $\text{N}_2$ , NMR samples were subjected to three freeze-pump-thaw cycles in a J Young tube before backfilling with Ar gas prior to data collection. Spectra were obtained following equilibration at the listed temperature for at least  $10\text{ min}$ . The hydride resonances are not shown.

hydride resonance (vide infra). We speculate that this apparent equivalence results from  $\text{N}_2$  ligand exchange between the two Fe sites. While slow decomposition of **3-N<sub>2</sub>** is observed at  $373\text{ K}$ , the Fe site equivalence was found to be reversible as cooling the sample back to  $293\text{ K}$  restored the spectrum of the remaining **3-N<sub>2</sub>**. The product(s) of the thermal decomposition of **3-N<sub>2</sub>** have not been ascertained despite our attempts to isolate and characterize them.

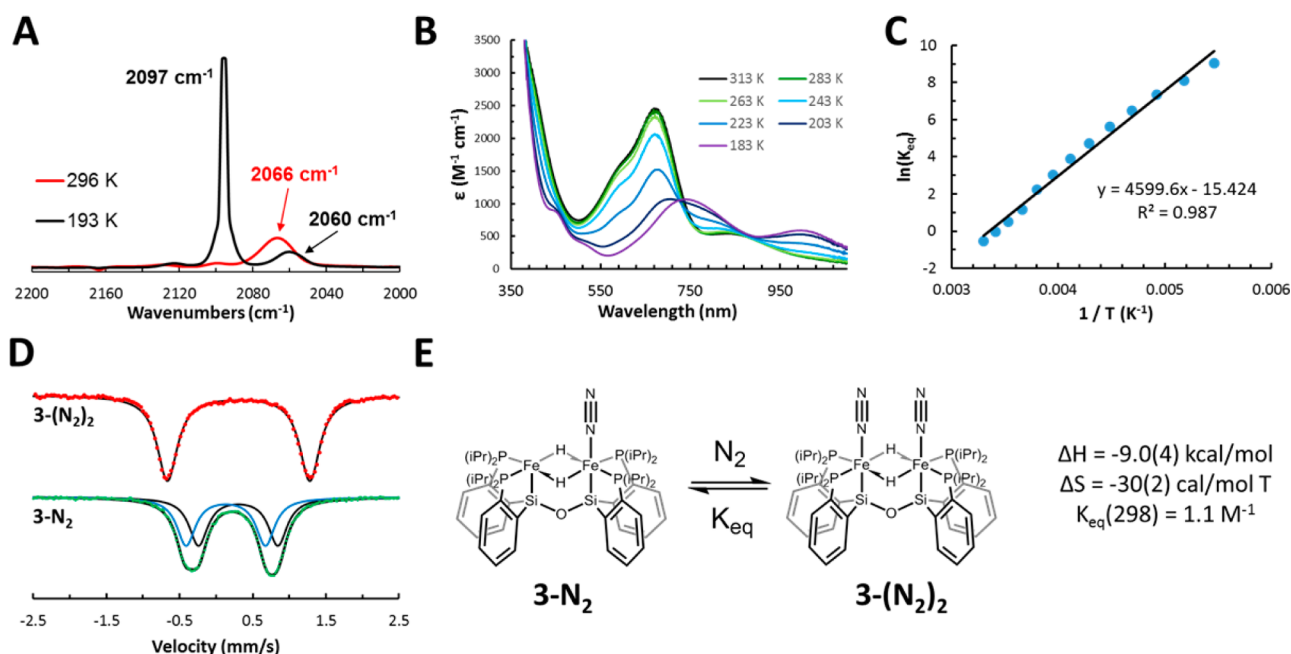


**Figure 3.** Spectroscopic observation of  $3-(N_2)_2$  at low temperatures. (A) Solution IR absorption spectra of  $3-N_2$  at 296 K (red) and  $3-(N_2)_2$  at 193 K (black) dissolved in  $N_2$ -saturated toluene. (B) UV–visible spectra of an  $N_2$ -saturated hexane solution of  $3-N_2/3-(N_2)_2$  at the listed temperatures. (C) Van't Hoff plot derived from the UV–visible spectral changes recorded at 675 nm and the published  $N_2$  solubility values in cryogenic hexane.<sup>18</sup> (D)  $^{57}Fe$  Mössbauer spectra (zero field, 80K) of polycrystalline  $3-N_2$  (bottom, green dots) and  $3-(N_2)_2$  in 2-MeTHF (top, red dots). The two subspectra of  $3-N_2$  shown are only one possible fit to the data (refer to Supporting Information for complete details). (E) Chemical equilibrium and thermodynamic parameters derived from the Van't Hoff analysis of the equilibrium  $N_2$ -binding process.

**$N_2$ -Binding Equilibria of  $3-N_2$ .** IR spectroscopy indicates that an additional  $N_2$  molecule coordinates to  $3-N_2$  at low temperatures in  $N_2$ -saturated solutions. At 298 K in toluene solution, a single  $\nu(N-N)$  vibration is observed at 2066  $cm^{-1}$  (Figure 3A) (KBr, 2062  $cm^{-1}$ ). Cooling this solution to 193 K results in the appearance of two features at 2097 and 2060  $cm^{-1}$ . Warming the solution back to 298 K results in the loss of these bands and reappearance of the 2066  $cm^{-1}$  vibration assigned to  $3-N_2$ . These data suggest that two  $N_2$  molecules are bound at low temperatures, forming a species denoted as  $3-(N_2)_2$ . The two vibrations observed at 193 K can be understood as symmetric and antisymmetric stretching modes derived from two coupled  $\nu(N-N)$  vibrations of similar energy. Frequency calculations on the optimized geometry of  $3-(N_2)_2$  (vide infra) bolster these assignments and closely match the intensity pattern observed (Supporting Information).



UV–visible spectroscopy was found to be a convenient tool for determining the thermodynamic parameters of  $N_2$  binding to the five-coordinate Fe site of  $3-N_2$ . Room temperature solutions of dilute  $3-N_2$  in  $N_2$ -saturated hexane display absorption bands centered at 600, 680, and 864 nm (Figure 3B) in the visible spectrum. On cooling, these bands decrease in intensity, concomitant with the appearance of prominent absorption bands at 750 and 1006 nm ascribable to  $3-(N_2)_2$ . Argon-saturated solutions of  $3-N_2$  do not display these features on cooling. The temperature-dependent spectral changes observed in  $N_2$ -saturated hexane solutions can be fit to provide the thermodynamic binding constant,  $K_{eq}$ , for  $N_2$  binding in eq 1.<sup>18</sup> A Van't Hoff analysis of the resulting data (Figure 3C) furnishes the pertinent thermodynamic parameters of this process. The large, negative entropy of bonding ( $-30(2)$  cal/

mol·K) is consistent with the coordination of a gas molecule,<sup>19</sup> and the rather small enthalpy of binding ( $-9.0(4)$  kcal/mol) is in line with the exclusive observation of  $3-(N_2)_2$  at low temperatures.

Zero-field  $^{57}Fe$  Mössbauer data (Figure 3D) corroborate the temperature-dependent nature of  $3-N_2$ . Solid  $3-N_2$  displays two broad features that can be fit with two quadrupole doublets in a 1:1 ratio, suggesting the presence of two distinct Fe environments. This is in accord with the solid-state structure of  $3-N_2$  and the NMR data in solution. The spectrum of  $3-(N_2)_2$ , prepared by dissolving  $^{57}Fe-3-N_2$  in  $N_2$ -saturated 2-MeTHF at 173 K followed by freezing at 77 K, reveals sharper features at different positions than that of  $3-N_2$ . This spectrum is well fit by a single Lorentzian quadrupole doublet, suggesting two equivalent Fe environments.

Fe K-edge extended X-ray absorption fine structure (EXAFS) measurements coupled to DFT calculations provide structural information on  $3-(N_2)_2$ . EXAFS data (Supporting Information) on  $3-(N_2)_2$  dissolved in a 2-MeTHF glass indicate an increased Fe...Fe distance (2.75(2) Å) relative to that found for solid  $3-N_2$  by EXAFS (2.47(2) Å) and XRD (2.4797(3) Å). The DFT-optimized geometry of  $3-N_2$  and  $3-(N_2)_2$  (BP86/6-31G(d)) are in agreement with the experimental data and reveal Fe...Fe distances of 2.494 and 2.729 Å, respectively. The calculated and experimental Fe–N and average Fe–P/Si distances were found to be similar in  $3-N_2$  and  $3-(N_2)_2$  (see Supporting Information for further details).

**Observation of a Low-lying Excited State in  $3-N_2$ .** In addition to the dynamic  $N_2$ -coordination behavior of  $3-N_2$  at low temperatures, NMR measurements suggest that this species has a thermally accessible paramagnetic excited state. At 293 K, an unusually upfield hydride resonance is observed for  $3-N_2$  at a chemical shift of  $\delta = -38.2$  ppm (Figure 4). Previously



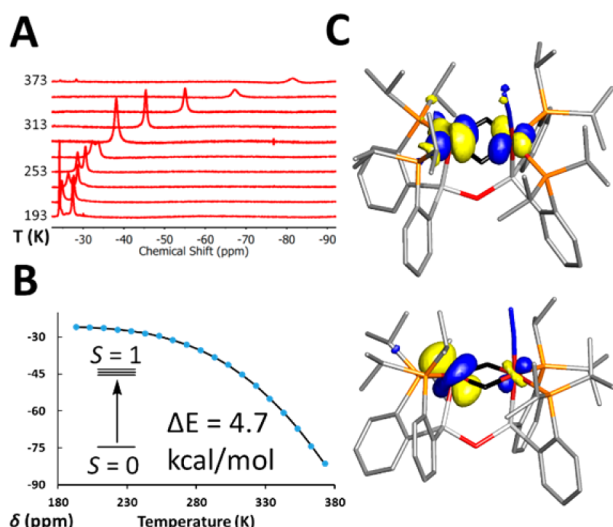


**Figure 4.** Temperature dependence of the Fe-( $\mu$ -H)-Fe chemical shift in  $3\text{-N}_2$  and thermal population of an excited triplet state. (A)  $^1\text{H}$  NMR spectra of  $3\text{-N}_2$  collected at the listed temperatures. (B) Fit of the  $^1\text{H}$  chemical shift of  $3\text{-N}_2$  to the magnetization equation defined in the Supporting Information. (C) Orbital surfaces of the two singly occupied (occupancy = 1.00) natural orbitals. All other orbitals had occupancies of  $>1.90$  or  $<0.10$  electrons.

reported Fe( $\mu$ -H)Fe complexes display hydride resonances in the region around  $-22$  ppm.<sup>20–22</sup> On cooling, this resonance resolves into two signals in a 1:1 ratio centered at  $\delta = -26.3$  ppm at 193 K. With increasing temperature, the average position of the hydride resonances smoothly decreases in a nonlinear fashion to  $\delta = -81.5$  ppm at 373 K. The temperature dependence of the average hydride chemical shift of  $3\text{-N}_2$  is not associated with  $\text{N}_2$  coordination to form  $3\text{-(N}_2)_2$ ; the hydride chemical shift is the same in  $\text{N}_2$ - and Ar-saturated solvents (at a given temperature), and the greatest changes in chemical shift are observed at temperatures where  $3\text{-N}_2$  predominates ( $K_{\text{eq}} \ll 1$ , eq 1). Such a dramatic temperature dependence of a metal-hydride chemical shift has been previously observed on  $\text{K}_2[\text{LNi}(\mu\text{-H})_2\text{Ni}(\mu\text{-H})_2\text{NiL}]$  ( $\text{L} = [\text{HC}(\text{CMeNC}_6\text{H}_3(\text{iPr})_2)_2]^-$ ) and attributed to partial thermal population of a paramagnetic excited state.<sup>23</sup> The hydride chemical shift of  $3\text{-N}_2$  is well fit to a magnetization function (Supporting Information), suggesting the presence of an excited state lying 4.7 kcal/mol above the ground state.

Single-point calculations (BP86/6-31G(d)) on the optimized geometries of  $3\text{-N}_2$  in singlet, triplet, and quintet spin states correctly locate a diamagnetic ground state with triplet and quintet states lying 4.4 and 21.1 kcal/mol higher in energy, respectively. We therefore attribute the temperature-dependent hydride chemical shift to partial thermal population of a triplet excited state. The singly occupied natural orbitals<sup>24</sup> of  $3\text{-N}_2$  optimized in a triplet spin state (Figure 4) illustrate that the unpaired spin density is delocalized over both Fe sites. However, the five-coordinate Fe site (spin density +1.96) bears more unpaired spin than the  $\text{N}_2$ -bound Fe site (spin density +0.43).

**Formation of a Mixed-Valent  $\text{Fe}_2(\mu\text{-H})_2$  Species.** Open-shell iron hydride species have been proposed as catalytically relevant in nitrogenase and other metalloenzymes.<sup>10,25–27</sup> As such, we explored the possibility of accessing paramagnetic Fe( $\mu$ -H)Fe species in this system. Briefly stirring  $3\text{-N}_2$  over an excess of Na(Hg) in the presence of 12-crown-4 in  $\text{N}_2$ -

saturated THF and subsequent workup affords  $\{\text{Na}(12\text{-crown-4})_2\}[\text{SiP}_2\text{O}]\text{Fe}_2(\mu\text{-H})_2(\text{N}_2)_2\}$  ( $4\text{-(N}_2)_2$ ).<sup>28</sup> The room temperature solution magnetic moment identifies  $4\text{-(N}_2)_2$  as an  $S = 1/2$  species ( $\mu_{\text{eff}} = 1.7 \mu_{\text{B}}$ ). The solid-state structure of  $4\text{-(N}_2)_2$  is shown in Figure 1. One  $\text{N}_2$  ligand is bound to each of the Fe sites in a terminal fashion, and the bridging hydrides can be located. Upon reduction, the Fe...Fe distance has increased to 2.8722(5) Å in  $4\text{-(N}_2)_2$ . In addition, the average Fe–H distances have slightly increased from 1.67(2) Å to 1.73(3) Å. Insignificant changes are observed in the average Fe–P, Fe–N, and N–N distances from  $3\text{-N}_2$  to  $4\text{-(N}_2)_2$ . IR measurements on solid  $4\text{-(N}_2)_2$  reveal two coupled  $\nu(\text{N-N})$  vibrations (2023 and 1979  $\text{cm}^{-1}$ ). The intensity pattern and spacing of these modes are similar to that observed for  $3\text{-(N}_2)_2$  in solution but display an average bathochromic shift of 78  $\text{cm}^{-1}$ .

The EPR spectrum of  $4\text{-(N}_2)_2$ , collected at 77 K in a 2-MeTHF glass (Figure 5), is slightly rhombic and dominated by

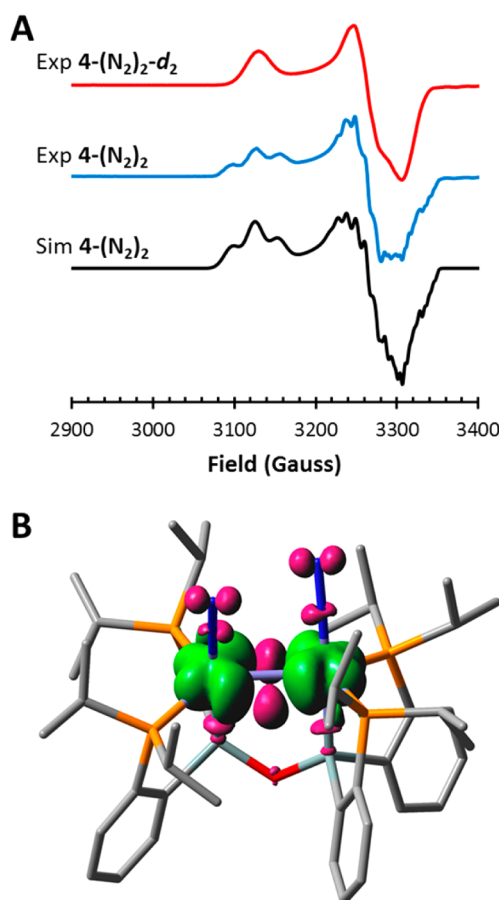


**Figure 5.** (A) X-band EPR spectra of  $4\text{-(N}_2)_2\text{-d}_2$  (red),  $4\text{-(N}_2)_2$  (blue) and the simulated EPR spectrum of  $4\text{-(N}_2)_2$ . Simulation parameters are listed in Table 1. Spectra were collected at 77 K in a 2-MeTHF glass at  $\nu = 9.395$  GHz at 2 mW power and modulation amplitude of 2 G. (B) Spin density plot of  $4\text{-(N}_2)_2$  shown with an isovalue of 0.0015.

features arising from hyperfine coupling. The spectrum can be simulated by considering three sets of two  $I = 1/2$  nuclei. The EPR spectrum of  $4\text{-(N}_2)_2\text{-d}_2$  does not display resolved hyperfine couplings, allowing the unambiguous assignment of the largest hyperfine coupling tensor to that arising from two equivalent bridging hydrides. The smaller values are therefore ascribed to two slightly different sets of  $^{31}\text{P}$  nuclei (Table 1). The spin density plot of  $4\text{-(N}_2)_2$  (Figure 5) shows a symmetric

Table 1. Select Spectroscopic Values Found for 4-(N<sub>2</sub>)<sub>2</sub>

axis	g	A( <sup>1</sup> H) <sup>a</sup>	A( <sup>31</sup> P <sub>a</sub> ) <sup>a</sup>	A( <sup>31</sup> P <sub>b</sub> ) <sup>a</sup>	A( <sup>57</sup> Fe) <sup>b</sup>
x	2.148	84	ND <sup>c</sup>	ND <sup>c</sup>	4.1
y	2.057	66	29	29	21
z	2.030	69	30	16	4.5

<sup>a</sup>Hyperfine tensor derived from the EPR spectrum, units in MHz.<sup>b</sup>Hyperfine tensor derived from the Mössbauer spectra, units in Tesla.<sup>c</sup>Not determined; coupling was not resolved due to line broadening.

distribution of unpaired spin density between the two Fe atoms. There is a notably high degree of spin polarization observed on the bridging hydride ligands, and this likely contributes to the large hyperfine coupling values observed in the EPR spectrum.

Mössbauer spectra of <sup>57</sup>Fe-enriched 4-(N<sub>2</sub>)<sub>2</sub> (5 K, 5 mM 2-MeTHF glass) collected in the presence of a small magnetic field (50 mT) display multiple broad features (Figure 6). The

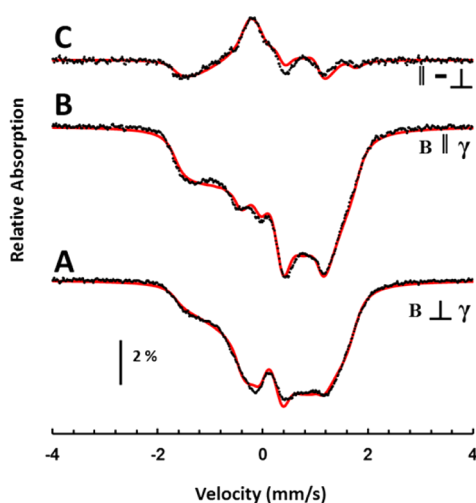


**Figure 6.** <sup>57</sup>Fe Mössbauer spectra recorded at 5 K on frozen 2-MeTHF solutions of 5 mM 4-(N<sub>2</sub>)<sub>2</sub> with a 50 mT magnetic field applied (A) perpendicular and (B) parallel to the propagation of the gamma beam. The difference spectrum is in (C). The experimental traces are in black and the simulated traces are shown in red.  $\delta = 0.35$  mm/s,  $\Delta E_Q = 0.69$  mm/s, and  $\eta = 0.86$  for 4-(N<sub>2</sub>)<sub>2</sub>. Refer to the Supporting Information for further details.

intensity of these features are dependent on the orientation of the magnetic field relative to that of the  $\gamma$ -beam, indicative of a slowly relaxing Kramers system.<sup>29</sup> The two spectra are well-simulated by an  $S = 1/2$  spin Hamiltonian,

$$\mathcal{H} = \mathbf{S} \cdot \mathbf{A} \cdot \mathbf{I} + \beta \mathbf{S} \cdot \mathbf{g} \cdot \mathbf{B} + \mathcal{H}_Q \quad (2)$$

including a magnetic hyperfine interaction, electronic Zeeman interaction, and the quadrupole interaction of the <sup>57</sup>Fe nucleus, respectively. The inclusion of an unidentified quadrupole doublet impurity accounting for 6% of the total Fe content resulted in the fit shown in Figure 6 (see Supporting Information for details). Good agreement between the experimental and simulated difference spectra validates the fit parameters listed in Table 1. Importantly, the simulation of 4-(N<sub>2</sub>)<sub>2</sub> shown is obtained by assuming that the spin Hamiltonian parameters for each Fe atom are identical, allowing the classification of 4-(N<sub>2</sub>)<sub>2</sub> as a class III mixed-valence ion.<sup>30</sup>

**Electrochemical Studies.** The chemical reduction of 3-N<sub>2</sub> at room temperature is coupled to the coordination of an

additional tightly bound N<sub>2</sub> ligand to form 4-(N<sub>2</sub>)<sub>2</sub>. In 4-(N<sub>2</sub>)<sub>2</sub>, the bound N<sub>2</sub> ligands are stable to multiple freeze–pump–thaw cycles, suggesting very strong binding to the two Fe sites. This is in contrast to that observed for 3-N<sub>2</sub>, where formation of 3-(N<sub>2</sub>)<sub>2</sub> is only observed at low temperatures. The inability to isolate 4-N<sub>2</sub> and measure its N<sub>2</sub> binding affinity directly prompted electrochemical experiments to quantify the binding affinity of 4-N<sub>2</sub>.

Cyclic voltammetry measurements on N<sub>2</sub>-saturated THF solutions of 3-(N<sub>2</sub>)<sub>2</sub> in THF electrolyte (Figure 7) recorded at 198 K reveal a reversible reduction event centered at  $-2.04$  V at all recorded scan rates (Figure 7A; features a and a'). Comparison of the UV–visible spectra collected at low temperature in hexane and THF confirm that 3-(N<sub>2</sub>)<sub>2</sub> is the predominant (>95%) species in THF solution at 198 K. This reversible electrochemical event can thus be assigned to the reduction of 3-(N<sub>2</sub>)<sub>2</sub> to 4-(N<sub>2</sub>)<sub>2</sub> (Figure 7D, eq 2). The large peak to peak splitting ( $\sim 1$  V at 2000 mV/s scan rate) results from the large solution resistance due to the low temperature and the weakly polar electrolyte solution employed.

The cyclic voltammograms obtained on 3-N<sub>2</sub> at room temperature suggest dynamic N<sub>2</sub> coordination behavior. UV–visible spectra collected in N<sub>2</sub>-saturated THF suggest that 3-N<sub>2</sub> is the predominant (>98%) neutral species at 298 K. Cyclic voltammograms recorded at slow scan rates at 298 K reveal an apparently reversible reduction event centered at  $-2.15$  V, slightly shifted from that observed at 198 K (features b and b'). At faster scan rates, new cathodic (denoted with c in Figure 7B) and anodic features (denoted with c' in Figure 7B) appear at more negative potentials.

A mechanistic model consistent with the available temperature- and scan-rate-dependent cyclic voltammetry data suggests two competing pathways by which 3-N<sub>2</sub> is converted to 4-(N<sub>2</sub>)<sub>2</sub>. The dominant pathway at slow scan rates appears to proceed through 3-(N<sub>2</sub>)<sub>2</sub>; this is manifest in a pseudoreversible wave observed at  $-2.15$  V (40 mV/s; 298 K). We infer that this wave reflects the 1-electron reduction of 3-(N<sub>2</sub>)<sub>2</sub> to 4-(N<sub>2</sub>)<sub>2</sub> (C–E mechanism).<sup>31</sup> Direct one-electron reduction of 3-N<sub>2</sub> to 4-N<sub>2</sub> requires more driving force and can be observed at faster scan rates. For instance, at 4000 mV/s the waveform shows two features (b and c) that reflect 3-N<sub>2</sub> to 4-N<sub>2</sub> (c) and 3-N<sub>2</sub> to 4-(N<sub>2</sub>)<sub>2</sub> (b) redox events. Rapid binding of N<sub>2</sub> to 4-N<sub>2</sub> to produce 4-(N<sub>2</sub>)<sub>2</sub> constitutes the second path by which 3-N<sub>2</sub> funnels to 4-(N<sub>2</sub>)<sub>2</sub> (E–C mechanism).

These N<sub>2</sub>-binding and redox processes are collectively depicted in the square scheme shown in Figure 7D. Simultaneously fitting the various scan rates obtained at 298 K furnishes the simulated waveforms (Figure 7C) and parameters (Figure 7E). The individual rate constants were allowed to freely float, but the equilibrium N<sub>2</sub>-binding constant for 3-N<sub>2</sub> was constrained to that found in hexane via UV–visible spectroscopy ( $K_{eq1} = 1.1$  M<sup>−1</sup>). Reduction potentials derived from the simulation for the two electrochemical processes agree well with those obtained by visual inspection of the voltammograms. The individual N<sub>2</sub>-binding rate constants are reasonable, and their magnitudes are within the range found for CO and O<sub>2</sub> binding to Fe(porphyrin) complexes.<sup>32</sup>

**Reduction of N<sub>2</sub> to NH<sub>3</sub> with H<sup>+</sup>/e<sup>−</sup> Equivalents.** While the catalytic conversion of N<sub>2</sub> to NH<sub>3</sub> by protons and electrons has now been established in mononuclear Fe and Mo systems,<sup>4,5,33,34</sup> this transformation in nitrogenase may be most efficiently catalyzed by the combined action of multiple

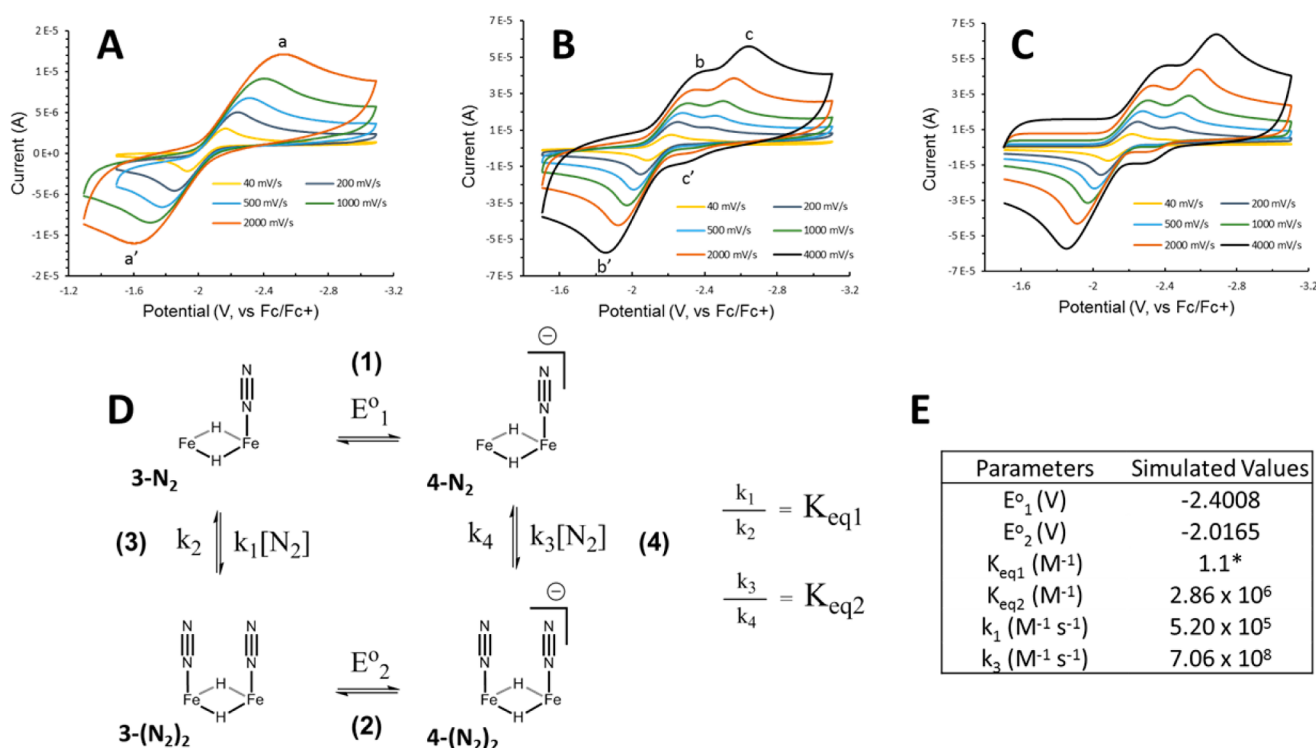


**Figure 7.** (A) Cyclic voltammetry measurements on  $N_2$ -saturated THF electrolyte solutions of  $3-(N_2)_2$  at 198 K. (B) Cyclic voltammograms obtained on solutions of  $3-N_2$  at 298 K. (C) Simulation of the voltammograms obtained at 298 K. (D) Square scheme model considered in the simulation traces shown in (C). Equations 1 and 2 represent the electrochemical reduction equilibria of  $3-N_2$  and  $3-(N_2)_2$ . Equations 3 and 4 represent the  $N_2$ -binding equilibria for  $3-N_2$  and  $4-N_2$ . The charges shown are representative of the full molecule. (E) Table listing critical parameters defined in the model and the resulting values found upon simulation. An asterisk denotes values that were held constant during the simulation. Refer to the Supporting Information for additional fit parameters.

metal sites. As such,  $3-N_2$  or  $4-(N_2)_2$  may serve as a platform to study the cooperative activation and reduction of  $N_2$  to  $NH_3$ . Analyses for the production of  $NH_3$  from  $N_2$  reveal the generation of  $1.4 \pm 0.5$  mol equiv of  $NH_3$  upon exposure of  $3-N_2$  to 48 equiv of  $KC_8$  and  $\{(Et_2O)_2H\}\{(3,5-(CF_3)_2-C_6H_3)_4B\}$  at  $-78^\circ C$  in diethyl ether. Lowering the  $H^+/e^-$  equivalents to 10 results in a diminished yield (0.51(9) equiv  $NH_3$ ). Very little  $NH_3$  (0.2(1) equiv) is detected when this experiment is repeated at  $0^\circ C$ . Use of  $4-(N_2)_2$  as a precatalyst also furnishes an appreciable yield of  $NH_3$  (1.1(2) equiv). The yields of  $NH_3$  produced per Fe atom in  $3-N_2$  are similar to that found for  $\{Na(12-crown-4)_2\}\{[SiP^{iPr}_3]Fe(N_2)\}$  (**5**) ( $[SiP^{iPr}_3] = (o-C_6H_4P(iPr)_2)_3Si(-)$ ) (0.7 equiv  $NH_3/Fe$ ). With respect to the individual Fe sites, the formal replacement of a phosphine ligand in **5** with a  $[Fe(\mu-H)_2]$  unit ( $3-N_2$ ) has little effect on the overall reaction efficiency. It is not clear whether the two Fe sites in  $3-N_2$  act cooperatively to effect  $N_2$  reduction or if the two sites act independently.

## DISCUSSION

In nitrogenase, mounting spectroscopic, enzymatic, and theoretical data suggest that one or more Fe centers are intimately involved in  $N_2$  reduction at FeMoco.<sup>1,35</sup> While molybdenum greatly enhances the efficiency of nitrogenase relative to FeVco and FeFeco congeners, its role in catalysis is unclear. Under a scenario where  $N_2$  coordinates to an Fe site of FeMoco, it is noteworthy that isolable terminal  $Fe-N_2$  species exclusively exhibit intermediate- or low-spin states and these species are further supported by strong-field ancillary ligands.<sup>7,36</sup> In this regard, the weak-field, sulfur-rich environ-

ment of FeMoco would seem unfit for the stabilization of locally low or intermediate spin Fe sites. Indeed, the FeMoco exhibits no affinity for  $N_2$  (or even CO) in the crystallographically characterized resting state of FeMoco, wherein the Fe sites are exclusively ligated to sulfide, thiolate, and carbide ligands.<sup>37–39</sup> At present, terminal  $Fe-N_2$  complexes supported by ligands of these types are unknown.<sup>15,40</sup>

Transient bridging hydride ligands purportedly accumulate in FeMoco under turnover conditions.<sup>1</sup> These hydride ligands have been proposed to store reducing equivalents on the cluster.<sup>41</sup> We are considering the possibility that accumulated hydride ligands may also play a critical role in adjusting the electronic properties of the cluster to support the coordination of  $N_2$  to an Fe center. The transient bridging hydrides on FeMoco may favor the formation of locally low or intermediate spin Fe ions, apt for  $N_2$  coordination and efficient nitrogenase activity. This hypothesis is rooted in the strong-field, electron-donating nature of *terminal* hydride ligands,<sup>9</sup> and the ability of these ligands to support the coordination of  $N_2$  to Fe.<sup>7,14</sup> Prior to this work, the coordination and subsequent functionalization of  $N_2$  at an  $Fe(\mu-H)Fe$  unit was without literature precedent. It is thus worthwhile to consider the spectroscopic, geometric, and thermodynamic properties of the compounds presented herein as model complexes for a bridging hydride-bound state of FeMoco.

The diiron compounds studied in this work are supported by strong-field phosphine, silyl, and hydride ligands. The observation of low-spin ground states in  $3-N_2$  and  $4-(N_2)_2$  is thus unsurprising and favors the terminal coordination of  $N_2$ , allowing for the complete characterization of these model



complexes. Unexpectedly, variable-temperature NMR experiments are consistent with a low-lying triplet excited state of  $3\text{-N}_2$  that is observed to lie 4.7 kcal/mol above the ground  $S = 0$  state. The five-coordinate geometry of FeI and the electron-deficient nature of the  $\text{Fe}_2(\mu\text{-H})_2$  core likely allow access to this state. This result underscores the propensity of coordinatively unsaturated Fe centers to populate higher spin configurations, even in strong-field, tetragonal ligand environments.<sup>42–44</sup>

Because a  $\text{N}_2$ -bound form of FeMoco has yet to be characterized, it is important to delineate the thermodynamic factors of  $\text{N}_2$ -coordination to synthetic, multimetallic platforms.<sup>45</sup> As the two Fe sites in  $3\text{-(N}_2)_2$  are identical, it is curious that one  $\text{N}_2$  ligand is lost on warming to room temperature. The accommodation of two  $\text{N}_2$  molecules in the substrate pocket of  $[\text{SiP}_2\text{O}]$  likely results in increased steric repulsion, rendering one  $\text{N}_2$  ligand labile. In addition, EXAFS data indicate that the formation of  $3\text{-(N}_2)_2$  from  $3\text{-N}_2$  is accompanied by a separation of the two Fe centers by ca. 0.3 Å. DFT-optimized geometries suggest that this elongation distorts the  $\text{Fe}_2(\mu\text{-H})_2$  rhomb and increases the average Fe–H distances by 0.04 Å. Combined with the aforementioned steric effects, the energetic penalty of reorganizing the  $\text{Fe}_2(\mu\text{-H})_2$  core manifests itself in the small overall enthalpy of  $\text{N}_2$  binding.

The chemical reduction of  $3\text{-N}_2$  is coupled to the coordination of  $\text{N}_2$  to form  $4\text{-(N}_2)_2$ , indicating much stronger binding of  $\text{N}_2$  to the reduced  $\text{Fe}_2(\mu\text{-H})_2$  core. The large equilibrium binding constant found for the coordination of  $\text{N}_2$  to the vacant site of  $4\text{-N}_2$  via electrochemical analysis supports this observation. Assuming that the entropy of  $\text{N}_2$  coordination to  $3\text{-N}_2$  and  $4\text{-N}_2$  is similar,<sup>46</sup> this dictates a much more negative enthalpy of  $\text{N}_2$  binding to  $4\text{-N}_2$  ( $\Delta H = -18$  kcal/mol) than to  $3\text{-N}_2$  ( $\Delta H = -9$  kcal/mol). The experimental difference in  $\text{N}_2$  binding enthalpy ( $\Delta\Delta H_{\text{exp}} = 9$  kcal/mol) between  $3\text{-N}_2$  and  $4\text{-N}_2$  agrees well with that predicted by DFT in the gas phase ( $\Delta\Delta H_{\text{DFT}} = 8$  kcal/mol).

The ability to reduce  $3\text{-(N}_2)_2$  without a large geometric distortion is remarkable as 36 valence electrons are present and reduction thus requires the occupation of an antibonding orbital. The electrochemical data collected on  $3\text{-N}_2$  suggest that at room temperature, electron transfer is preceded by the coordination of  $\text{N}_2$  to produce  $4\text{-(N}_2)_2$ , necessitating the intermediacy of  $3\text{-(N}_2)_2$ . The SOMO's of  $4\text{-N}_2$  and  $4\text{-(N}_2)_2$  are spatially very similar (Supporting Information) and are formally described as Fe–Fe  $\pi$ -antibonding. This orbital is *less* antibonding in  $4\text{-(N}_2)_2$  than in  $4\text{-N}_2$  as a result of the larger separation between the Fe sites (2.839 Å in  $4\text{-(N}_2)_2$ , 2.632 Å in  $4\text{-N}_2$ , DFT-optimized geometries). This analysis helps to rationalize why the reduction of  $3\text{-(N}_2)_2$  to  $4\text{-(N}_2)_2$  is accessed at much more positive potentials than for  $3\text{-N}_2$  to  $4\text{-N}_2$ : the  $\text{Fe}_2(\mu\text{-H})_2$  core in  $3\text{-(N}_2)_2$  is preorganized for electron transfer as the LUMO is nearly nonbonding with respect to the two Fe centers.

The electrochemical data obtained for this system suggests that the mixed-valent  $4\text{-N}_2$  displays a  $10^6$ -fold enhancement of  $\text{N}_2$ -binding affinity over  $3\text{-N}_2$ . The SOMO of  $4\text{-(N}_2)_2$  and also  $4\text{-N}_2$  is mostly centered on the two Fe atoms and nonbonding with respect to the  $\text{N}_2$  ligands. Population of this orbital serves to raise the energy of the occupied d-orbitals, enhancing the  $\pi$ -backbonding interaction with the bound  $\text{N}_2$  ligands. We suspect that the reason for the increased  $\text{N}_2$  binding affinity of  $4\text{-N}_2$  compared to  $3\text{-N}_2$  results from (i) the formal reduction of the Fe centers, increasing their ability to  $\pi$ -backbond into the N–N  $\pi$ -manifold, and (ii) the concomitant increase in Fe–Fe

separation upon reduction, which relaxes some steric pressure for the binding of the second  $\text{N}_2$  equivalent. These two factors are difficult to distinguish from one another. We note that the presence of a low-spin, formally  $d^7$  metal center in a pseudo-octahedral ligand environment is unusual but is made possible by bridging hydride ligands.<sup>47</sup> The bridging hydride ligands in the present system render the LUMO of  $3\text{-(N}_2)_2$  nonbonding with respect to the Fe–H bonds and thus chemically accessible.

Open-shell  $\text{Fe}(\mu\text{-H})\text{Fe}$  species have been proposed in a number of metalloenzymes, and well-characterized synthetic examples are rare.<sup>47–50</sup> Moreover, the precise location of the transient hydrides found on FeMoco are unknown.<sup>10</sup> The hydride-bound intermediate displays hyperfine coupling ( $A_{\text{iso}} \sim 23$  MHz) to two chemically equivalent hydrogen atoms that were assigned as hydride ligands bridging unspecified Fe atoms.<sup>51</sup> One possible structure considered by the authors was that of a  $\text{Fe}_2(\mu\text{-H})_2$  unit. The isolation of  $4\text{-(N}_2)_2$  allows for the spectroscopic parameters of a structurally well-defined  $\text{Fe}^{1.5}_2(\mu\text{-H})_2$  core to be defined and tested against those of the cluster. X-band EPR data on  $4\text{-(N}_2)_2$  reveal large hyperfine coupling ( $^1A_{\text{iso}} = 73$  MHz) to the bridging hydride ligands. The large  $^1A_{\text{iso}}$  value for  $4\text{-(N}_2)_2$  relative to the hydride-bound intermediate is expected because in  $4\text{-(N}_2)_2$  the total unpaired spin density is spread out over fewer atoms than in the large, spin-coupled FeMoco cluster. The spin-dipolar term,  $^1T = [11, -7, -4]$  (MHz) in  $4\text{-(N}_2)_2$  is nearly axial and distinct from the rhombic term found for the hydride-bound FeMoco intermediate  $[-13.3, 0.7, 12.7]$ .<sup>10</sup> Definitive conclusions correlating  $4\text{-(N}_2)_2$  as a model of the hydride-bound intermediate are premature and require comparative ENDOR experiments and analyses that will be the subject of a future study.<sup>45</sup>

## CONCLUDING REMARKS

Transient hydride ligands bridging two or more iron centers purportedly accumulate on the iron–molybdenum cofactor (FeMoco) of nitrogenase, and their role(s) in the reduction of  $\text{N}_2$  to  $\text{NH}_3$  remains unknown. We have suggested herein that one role these hydrides may serve is to facilitate  $\text{N}_2$  coordination at an iron site of FeMoco. We have considered this hypothesis in the context of a diiron model system supported by two bridging hydride ligands. Most noteworthy, these compounds bind either one or two molecules of  $\text{N}_2$  depending on the redox state of the  $\text{Fe}_2(\mu\text{-H})_2$  unit. An unusual example of a mixed-valent  $\text{Fe}^{\text{II}}(\mu\text{-H})_2\text{Fe}^{\text{I}}$  has been described that displays a  $10^6$ -fold enhancement of  $\text{N}_2$  binding affinity over its oxidized congener, estimated by spectroscopic and electrochemical techniques. This result underscores the dramatic impact a single electron-transfer (ET) step can play in terms of substrate binding. Moreover, the model system points to the possibility that binding one molecule of substrate ( $\text{N}_2$ ) can serve to facilitate an ET step and concomitant binding of a second equivalent of substrate. Finally, the compounds described here show promise as functional models of nitrogenase as substantial amounts of  $\text{NH}_3$  are produced upon exposure to proton and electron equivalents. Design improvements are needed to turn binucleating iron scaffolds of these types into functional catalysts.

## EXPERIMENTAL SECTION

**General Considerations.** All manipulations were carried out using standard Schlenk or glovebox techniques under an  $\text{N}_2$  or Ar atmosphere where noted. Unless otherwise noted, solvents were

deoxygenated and dried by thoroughly sparging with N<sub>2</sub> gas followed by passage through an activated alumina column in the solvent purification system by SG Water, LLC, USA. Nonhalogenated solvents were tested with a standard purple solution of sodium benzophenone ketyl in tetrahydrofuran in order to confirm effective oxygen and moisture removal. All reagents were purchased from commercial vendors and used without further purification unless otherwise stated. Bis(2-diisopropylphosphinophenyl)-chlorosilane (**1**),<sup>7</sup> [H(Et<sub>2</sub>O)<sub>2</sub>]-[(3,5-(CF<sub>3</sub>)<sub>2</sub>C<sub>6</sub>H<sub>3</sub>)<sub>4</sub>B],<sup>52</sup> K<sub>2</sub>C<sub>8</sub>,<sup>53</sup> [Cp<sub>2</sub>Fe][PF<sub>6</sub>],<sup>54</sup> and anhydrous <sup>57</sup>FeCl<sub>2</sub><sup>55</sup> were synthesized following literature procedures. Deuterated solvents were purchased from Cambridge Isotope Laboratories, Inc., degassed, and dried over NaK alloy then vacuum-transferred onto activated 3 Å molecular sieves prior to use. D<sub>2</sub> was freed of residual H<sub>2</sub>O and O<sub>2</sub> by passage through a coiled trap maintained at 77K prior to use. Elemental analyses were performed by Robertson Microlit Laboratories, Ledgebrook, NJ. <sup>1</sup>H, <sup>13</sup>C, and <sup>29</sup>Si chemical shifts are reported in ppm relative to tetramethylsilane, using residual solvent resonances as internal standards. <sup>31</sup>P chemical shifts are reported in ppm relative to 85% aqueous H<sub>3</sub>PO<sub>4</sub>. Solution phase magnetic measurements were performed by the method of Evans.<sup>56</sup> Near-infrared spectra were obtained on a Nicolet FT-NIR spectrometer using quartz cuvettes capped with a Teflon screw cap. X-band EPR spectra were obtained on a Bruker EMX spectrometer on 5 mM solutions prepared as frozen glasses in 2-MeTHF. EPR spectra were simulated using the EasySpin suite of programs with Matlab 2014.<sup>57</sup>

**IR Spectroscopy.** KBr-IR measurements were obtained on a Bio-Rad Excalibur FTS 3000 spectrometer. Thin-film and room temperature solution-phase IR were obtained on a Bruker Alpha spectrometer equipped with a diamond ATR probe. Variable-temperature solution IR spectra were acquired with the use of a SpecAc cryostat mounted within the Bio-Rad spectrometer.

**Optical Spectroscopy.** Measurements were taken on a Cary 50 UV–vis spectrophotometer using a 1 cm quartz cell connected to a round-bottom flask and sealed with a Teflon stopcock. Variable temperature measurements were collected with a Unisoku CoolSpek cryostat mounted within the Cary spectrophotometer. N<sub>2</sub>-binding equilibrium data were collected after the temperature of the cryostat was maintained at the desired temperature for at least 5 min.

**X-ray Crystallography.** XRD studies were carried out at the Beckman Institute Crystallography Facility on a Bruker Kappa Apex II diffractometer (Mo K $\alpha$  radiation). Structures were solved using SHELXS and refined against F<sup>2</sup> on all data by full-matrix least-squares with SHELXL. The crystals were mounted on a glass fiber under Paratone N oil.

**Electrochemistry.** Electrochemical measurements were carried out in a thick-walled single-compartment electrochemical cell fitted with a Teflon stopcock and tungsten leads protruding from the top of apparatus. A CH Instruments 600B electrochemical analyzer was used for data collection. A freshly polished 0.071 cm<sup>2</sup> diameter glassy carbon electrode (CH Instruments) was used as the working electrode, and platinum wire was used as the auxiliary electrode. The reference electrode was a Ag/AgNO<sub>3</sub> (1 mM)/THF nonaqueous reference electrode (also contained 0.1 M tetra-*n*-butylammonium hexafluorophosphate) separated from the solution by a Vycor frit (Bioanalytical Systems, Inc.). Solutions (THF) of electrolyte (0.1 M tetra-*n*-butylammonium hexafluorophosphate) contained ferrocene (1 mM), to serve as an internal reference, and analyte (1 mM). All reported potentials are referenced to the ferrocene couple, Cp<sub>2</sub>Fe<sup>+</sup>/Cp<sub>2</sub>Fe. All solutions were prepared under an N<sub>2</sub> atmosphere. Cyclic voltammograms were simulated with the DigiElch 7.0 software package.

**<sup>57</sup>Fe Mössbauer Spectroscopy.** Spectra were recorded on a spectrometer from SEE Co. (Edina, MN) operating in the constant acceleration mode in a transmission geometry. The sample was kept in an SVT-400 cryostat from Janis (Wilmington, MA). The quoted isomer shifts are relative to the centroid of the spectrum of a metallic foil of  $\alpha$ -Fe at room temperature. Solid samples were prepared by grinding polycrystalline material into a fine powder and then mounted in a Delrin cup fitted with a screw-cap as a boron nitride pellet. Solution samples were transferred to a sample cup chilled to 77K

inside of the glovebox. Upon freezing of the solution, the cup was quickly removed from the glovebox and immersed in liquid N<sub>2</sub> until being mounted in the cryostat. Data analysis was performed using the program WMOSS (www.wmoss.org) and quadrupole doublets were fit to Lorentzian lineshapes.

**EXAFS.** XAS data were collected in fluorescence mode at  $\sim$ 10K with a 30-element germanium detector (SSRL, BL7-3) using a Si(220)  $\Phi = 90^\circ$  double monochromator with a 9.5 keV cutoff for harmonic rejection. Photoreduction of the samples was not observed on subsequent scans (exposure time  $\sim$ 20 min per scan). Background removal and curve fitting were performed with EXAFSPAK (available at www-ssrl.slac.stanford.edu/exafspak.html). Data sets were fit over the range  $k = 2\text{--}12 \text{ \AA}^{-1}$ . A cobalt impurity in the slits prevented accurate fits over a wider range. All distances,  $R$ , and Debye–Waller factors,  $\sigma^2$ , were treated as adjustable parameters, and all threshold energy shifts,  $E_0$ , were linked but allowed to vary. The passive electron reduction factor,  $S_0$ , was fixed at 0.9.

**DFT Calculations.** Geometry optimizations, single-point calculations, frequency calculations, and NO analyses were performed using the Gaussian03 suite of programs (refer to Supporting Information for the complete reference) with the BP86 level of theory and a 6-31G(d) basis set for all atoms.

**[SiP<sub>2</sub>O]H<sub>2</sub> (**2**).** In the glovebox, a 100 mL Schlenk flask equipped with a Teflon stopper was charged with compound **1** (14.8 g, 32.8 mmol), triethylamine (3.5 g, 34.6 mmol), toluene (20 mL), and a magnetic stir bar. The flask was sealed and brought out of the glovebox. The clear solution was stirred, and water (300  $\mu$ L, 16.65 mmol) was added via micropipette in one portion under a backflow of N<sub>2</sub>. A white solid immediately precipitated. The flask was sealed and heated to 100 °C for 3 days. The solution was subsequently cooled to rt and filtered through a coarse frit in the glovebox, leaving [HNEt<sub>3</sub>][Cl] (4.40 g, 32.0 mmol, 97%). The filtrate was concentrated to dryness in vacuo and triturated with hexamethyldisiloxane (2  $\times$  2 mL) and concentrated, yielding an off-white oily solid. This solid was suspended in 10 mL of hexamethyldisiloxane, and the resulting suspension was stirred for 5 min and then cooled to  $-78^\circ\text{C}$  and filtered through a coarse frit, leaving compound **2** as a white solid (9.44 g, 11.1 mmol, 68%). The mother liquor was concentrated to 2 mL and stored at  $-35^\circ\text{C}$ , resulting in the slow formation of crystalline **2** (1.26 g, 1.5 mmol, 77% total yield). <sup>1</sup>H NMR (500 MHz, C<sub>6</sub>D<sub>6</sub>, 25 °C, ppm):  $\delta$  7.93 (d, 4H, Ar-H), 7.34 (d, 4H, Ar-H), 7.16 (t, 4H, Ar-H), 7.11 (m, 6H, Ar-H + Si-H), 2.03 (m, 4H, methine C-H), 1.92 (m, 4H, methine C-H), 1.08 (m, 24H, methyl C-H), 0.85 (m, 24H methyl C-H). <sup>31</sup>P{<sup>1</sup>H} NMR (202.4 MHz, C<sub>6</sub>D<sub>6</sub>, 25 °C, ppm):  $\delta$   $-0.50$  (s). <sup>29</sup>Si{<sup>1</sup>H} NMR (99.3 MHz, C<sub>6</sub>D<sub>6</sub>, 25 °C, ppm):  $\delta$   $-30.42$  (t,  $J_{\text{Si-P}} = 27.7$  Hz). <sup>13</sup>C{<sup>1</sup>H} NMR (125.7 MHz, C<sub>6</sub>D<sub>6</sub>, 25 °C, ppm):  $\delta$  146.98 (dd,  $J = 43.0$  Hz,  $J = 2.6$  Hz), 143.78 (d,  $J = 16.75$  Hz), 137.48 (d,  $J = 16.0$  Hz), 131.64 (d,  $J = 1.8$  Hz), 128.99 (s), 128.35 (s), 25.21 (t, 14.5 Hz), 20.85 (d,  $J = 14.4$  Hz), 20.63 ( $J = 18.7$  Hz), 20.21 (t,  $J = 11.2$  Hz). IR (KBr):  $\nu$ (Si-H) = 2199, 2166 cm<sup>-1</sup>.

**[SiP<sub>2</sub>O]Fe<sub>2</sub>( $\mu$ -H)<sub>2</sub>(N<sub>2</sub>) (**3-N<sub>2</sub>**).** In the glovebox, a 100 mL Schlenk flask was charged with compound **2** (2.00 g, 2.36 mmol), FeBr<sub>2</sub> (1.02 g, 4.72 mmol), THF (50 mL), and a magnetic stir bar. The solution was stirred vigorously at room temperature for 3 h, resulting in a clear pale-orange solution. Solvent was evaporated to dryness in vacuo, and Et<sub>2</sub>O (50 mL) was added to the resulting residue. The Schlenk tube was sealed and the suspension was vigorously stirred for 2 h at rt, producing a fine powder. Solvent was evaporated in vacuo, and the beige powder was subsequently dried under dynamic vacuum for 1 h. Freshly prepared Na(Hg) amalgam (0.217 g Na, 9.44 mmol, 20 g Hg) and a 1:1 mixture of pentane:Et<sub>2</sub>O (75 mL) was added to the flask, and vigorous stirring was commenced. The suspension was stirred overnight at room temperature, resulting in the deposition of ample gray precipitate and a solution color change to dark green. The mixture was filtered through Celite, and the solids were washed with Et<sub>2</sub>O (2  $\times$  25 mL). The filtrate was evaporated in vacuo and pentane (10 mL) was added subsequently, resulting in the slow precipitation of green solid. The solution was decanted, and the solid was washed with additional pentane (2  $\times$  5 mL) furnishing 1.40 g of **3-N<sub>2</sub>** (60% yield). <sup>1</sup>H NMR (500 MHz, C<sub>6</sub>D<sub>6</sub>, 25 °C, 1 atm N<sub>2</sub>, ppm):  $\delta$  8.44 (bs, 4H,



Ar-H), 8.11 (bs, 4H, Ar-H), 7.26 (bs, 4H, Ar-H), 6.90 (bs, 4H, Ar-H), 2.79 (bs, 2H, methine C-H), 2.41 (bs, 2H, methine C-H), 2.12 (bs, 2H, methine C-H), 1.95 (bs, 2H, methine C-H), 1.45 (bs, 12H, methyl C-H), 1.07 (bs, 24H methyl C-H), 0.56 (bs, 12H methyl C-H),  $-39.9$  (bs, 2H Fe( $\mu$ -H)Fe).  $^{31}\text{P}\{^1\text{H}\}$  NMR (202.4 MHz,  $\text{C}_6\text{D}_6$ , 25 °C, ppm):  $\delta$  112.6, 90.2, 80.7. UV-vis (hexane, 298 K, nm  $\{\text{cm}^{-1} \text{ M}^{-1}\}$ ): 400 {2900}, 600 {1600}, 680 {2450}. Anal Calcd for  $\text{C}_{48}\text{H}_{74}\text{Fe}_2\text{O}_4\text{P}_2\text{Si}_3$ : C, 58.42; H, 7.56; N, 2.84. Found: C, 58.16; H, 7.42; N, 2.68. IR (KBr):  $\nu(\text{N}-\text{N}) = 2062 \text{ cm}^{-1}$ .

**$[\text{SiP}_2\text{O}]\text{Fe}_2(\mu\text{-D})_2(\text{N}_2)$  ( $3\text{-N}_2\text{-d}_2$ ).** A 100 mL Schlenk flask was charged with  $3\text{-N}_2$  (78 mg, 79  $\mu\text{mol}$ ), pentane (20 mL), and a magnetic stirbar. The flask was sealed, chilled to 77 K, and the head space was evacuated for 5 min and then resealed and allowed to warm to room temperature. This process was repeated two more times. The flask was subsequently backfilled with 1 atm of  $\text{D}_2$ , sealed, and stirred at room temperature for 1 h, causing no detectable color change. The volatiles were then removed in vacuo, and the remaining residue was redissolved in toluene (5 mL) under an  $\text{N}_2$  atmosphere, filtered into a 20 mL scintillation vial, and then concentrated to dryness in vacuo. Minimal pentane (1 mL) was subsequently added to dissolve the green residue, and this solution was allowed to stand overnight, depositing green crystals of  $3\text{-N}_2\text{-d}_2$  (43 mg, 43  $\mu\text{mol}$ , 55%). Except for the hydride resonance, the  $^1\text{H}$  NMR of  $3\text{-N}_2\text{-d}_2$  looked identical to  $3\text{-N}_2$ . The residual hydride signal was integrated to verify that >95% of  $3\text{-N}_2$  was converted to  $3\text{-N}_2\text{-d}_2$ .

**$[\text{SiP}_2\text{O}]^{57}\text{Fe}_2(\mu\text{-H})_2(\text{N}_2)$  ( $^{57}\text{Fe-3-N}_2$ ).** In the glovebox, a 20 mL scintillation vial was charged with compound 2 (104 mg, 123  $\mu\text{mol}$ ),  $\text{FeBr}_2$  (26.7 mg, 124  $\mu\text{mol}$ ),  $^{57}\text{FeCl}_2$  (15.8 mg, 125  $\mu\text{mol}$ ), THF (10 mL), and a magnetic stir bar. The solution was stirred vigorously at room temperature for 3 h, resulting in a clear pale-orange solution. Solvent was evaporated to dryness in vacuo, and  $\text{Et}_2\text{O}$  (10 mL) was added to the resulting residue. The scintillation vial was capped and the suspension was vigorously stirred for 1 h at rt, producing a fine powder. Solvent was evaporated in vacuo, and the beige powder was subsequently dried under dynamic vacuum for 1 h. Freshly prepared Na(Hg) amalgam (11.5 mg Na, 500  $\mu\text{mol}$ , 2.3 g Hg) suspended in a 1:1 mixture of pentane: $\text{Et}_2\text{O}$  (10 mL) was added to the flask, and vigorous stirring was commenced. The suspension was stirred for 4 h at room temperature, resulting in the deposition of ample gray precipitate and a solution color change to dark green. The mixture was filtered through Celite, and the solids were washed with  $\text{Et}_2\text{O}$  ( $2 \times 5$  mL). The filtrate was evaporated in vacuo and pentane (2 mL) was added subsequently, resulting in the slow precipitation of green solid. The solution was decanted, and the solid was washed with additional pentane ( $3 \times 2$  mL). The green solid was dissolved in toluene (2 mL), filtered, and evaporated to dryness in vacuo. The residue was dissolved in pentane (2 mL) and allowed to stand overnight, resulting in the precipitation of crystalline  $^{57}\text{Fe-3-N}_2$  (53.2 mg, 44% yield). The  $^1\text{H}$  NMR looked identical to  $3\text{-N}_2$ . The level of  $^{57}\text{Fe}$  incorporation was not explicitly determined.

**$\{\text{Na}(12\text{-Crown-4})_2\}[\text{SiP}_2\text{O}]\text{Fe}_2(\mu\text{-H})_2(\text{N}_2)_2$  ( $4\text{-(N}_2)_2$ ).** In a glovebox, a 20 mL scintillation vial was charged with sodium (4.5 mg, 196  $\mu\text{mol}$ ), mercury (2.45g), a solution of 12-crown-4 (50 mg, 284  $\mu\text{mol}$ ) in THF (5 mL), and a magnetic stir bar. The vial was capped and stirred vigorously for 5 min, resulting in a finely divided Na(Hg) suspension. The vial was uncapped and complex  $3\text{-N}_2$  (104.1 mg, 105  $\mu\text{mol}$ ) was added in one portion. The vial was vigorously stirred for 3 min, resulting in a color change to a very dark amber. This solution was filtered and evaporated to dryness in vacuo. The residue was thoroughly digested with pentane (5 mL), which was subsequently decanted. The resulting dark-brown microcrystals were additionally washed with 2:1 pentane: $\text{Et}_2\text{O}$  (5 mL) and then pentane (2 mL). Residual solvent was evaporated in vacuo, leaving 141 mg of  $4\text{-(N}_2)_2$  (98% yield).  $^1\text{H}$  NMR (300 MHz, THF- $d_8$ , 25 °C, 1 atm  $\text{N}_2$ , ppm):  $\delta$  7.38, 3.78,  $-2.12$ . UV-vis-NIR (2-MeTHF, 298 K, nm  $\{\text{cm}^{-1} \text{ M}^{-1}\}$ ): 645 {1800}, 960 {600}, 1075 {300}, 1410 {150}. IR (KBr):  $\nu(\text{N}-\text{N}) = 2023 \text{ cm}^{-1}$ ,  $1979 \text{ cm}^{-1}$ .  $\mu_{\text{eff}}$  (THF- $d_8$ , Evans method, 20 °C): 1.7  $\mu_{\text{B}}$ .

**Typical  $\text{NH}_3$  Generation Protocol.**  $3\text{-N}_2$  (2 mg, 0.002 mmol) was dissolved in  $\text{Et}_2\text{O}$  (0.5 mL) in a 50 mL Schlenk tube equipped with a stir bar. This suspension was vigorously stirred and cooled to  $-78$  °C

in a cold well inside of the glovebox. A similarly cooled solution of  $[\text{H}(\text{Et}_2\text{O})_2][(\text{3,5-(CF}_3)_2\text{C}_6\text{H}_3)_4\text{B}]$  (93 mg, 0.092 mmol) in  $\text{Et}_2\text{O}$  (1.0 mL) was added to the suspension in one portion with rapid stirring. Any remaining acid was dissolved in cold  $\text{Et}_2\text{O}$  (0.5 mL) and added subsequently. The reaction mixture turned orange upon addition of acid. Solid  $\text{KCl}$  (15 mg, 0.100 mmol) was suspended in cold  $\text{Et}_2\text{O}$  (0.75 mL) and added in one portion to the rapidly stirred solution in the Schlenk tube, which was then tightly sealed. The reaction was allowed to stir for 40 min at  $-78$  °C before being warmed to room temperature and stirred for 15 min.

**Ammonia Quantification.** A Schlenk tube was charged with HCl (3 mL of a 2.0 M solution in  $\text{Et}_2\text{O}$ , 6 mmol). Reaction mixtures were vacuum transferred into this collection flask. Residual solid in the reaction vessel was treated with a solution of  $[\text{Na}][\text{O-}t\text{-Bu}]$  (40 mg, 0.4 mmol) in 1,2-dimethoxyethane (1 mL) and sealed. The resulting suspension was allowed to stir for 10 min before all volatiles were again vacuum transferred into the collection flask. After completion of the vacuum transfer, the flask was sealed and warmed to room temperature. Solvent was removed in vacuo, and the remaining residue was dissolved in  $\text{H}_2\text{O}$  (1 mL). An aliquot of this solution (40  $\mu\text{L}$ ) was then analyzed for the presence of  $\text{NH}_3$  (trapped as  $[\text{NH}_4][\text{Cl}]$ ) via the indophenol method.<sup>58</sup> Quantification was performed with UV-visible spectroscopy by analyzing the absorbance at 635 nm.

## ■ ASSOCIATED CONTENT

### ● Supporting Information

Additional experimental details, spectra, X-ray crystallographic information (CIF) and DFT coordinates. This material is available free of charge via the Internet at <http://pubs.acs.org>.

## ■ AUTHOR INFORMATION

### Corresponding Author

[jpeters@caltech.edu](mailto:jpeters@caltech.edu)

### Notes

The authors declare no competing financial interest.

## ■ ACKNOWLEDGMENTS

This work was supported by the N.I.H. (GM 070757) and the Gordon and Betty Moore Foundation. J.R. was supported by an N.S.F. graduate research fellowship. We thank Larry Henling for crystallographic assistance, Prof. Michael T. Green and Elizabeth Onderko for assistance with the collection and analysis of EXAFS data, Dr. Angelo di Bilio for assistance with EPR measurements, and Prof. George Rossman for assisting with near-IR spectrophotometry measurements.

## ■ REFERENCES

- (1) Hoffman, B. M.; Lukoyanov, D.; Dean, D. R.; Seefeldt, L. C. *Acc. Chem. Res.* **2013**, *46*, 587.
- (2) Lee, H. I.; Igarashi, R. Y.; Laryukhin, M.; Doan, P. E.; Dos Santos, P. C.; Dean, D. R.; Seefeldt, L. C.; Hoffman, B. M. *J. Am. Chem. Soc.* **2004**, *126*, 9563.
- (3) George, S. J.; Barney, B. M.; Mitra, D.; Igarashi, R. Y.; Guo, Y. S.; Dean, D. R.; Cramer, S. P.; Seefeldt, L. C. *J. Inorg. Biochem.* **2012**, *112*, 85.
- (4) Anderson, J. S.; Rittle, J.; Peters, J. C. *Nature* **2013**, *501*, 84.
- (5) Creutz, S. E.; Peters, J. C. *J. Am. Chem. Soc.* **2014**, *136*, 1105.
- (6) Rodriguez, M. M.; Bill, E.; Brennessel, W. W.; Holland, P. L. *Science* **2011**, *334*, 780.
- (7) Takaoka, A.; Mankad, N. P.; Peters, J. C. *J. Am. Chem. Soc.* **2011**, *133*, 8440.
- (8) Bart, S. C.; Lobkovsky, E.; Bill, E.; Wieghardt, K.; Chirik, P. J. *Inorg. Chem.* **2007**, *46*, 7055.
- (9) Chatt, J.; Hayter, R. G. *J. Chem. Soc.* **1961**, 772.

- (10) Igarashi, R. Y.; Laryukhin, M.; Dos Santos, P. C.; Lee, H. I.; Dean, D. R.; Seefeldt, L. C.; Hoffman, B. M. *J. Am. Chem. Soc.* **2005**, *127*, 6231.
- (11) Lowe, D. J.; Thorneley, R. N. F. *Biochem. J.* **1984**, *224*, 877.
- (12) Yang, Z. Y.; Khadka, N.; Lukoyanov, D.; Hoffman, B. M.; Dean, D. R.; Seefeldt, L. C. *Proc. Natl. Acad. Sci. U. S. A.* **2013**, *110*, 16327.
- (13) Ghilardi, C. A.; Midollini, S.; Sacconi, L.; Stoppioni, P. *J. Organomet. Chem.* **1981**, *205*, 193.
- (14) Vandersluys, L. S.; Eckert, J.; Eisenstein, O.; Hall, J. H.; Huffman, J. C.; Jackson, S. A.; Koetzle, T. F.; Kubas, G. J.; Vergamini, P. J.; Caulton, K. G. *J. Am. Chem. Soc.* **1990**, *112*, 4831.
- (15) Allen, F. H. *Acta Crystallogr., Sect. B: Struct. Sci.* **2002**, *58*, 380.
- (16) A single, broad resonance is observable in the  $^{29}\text{Si}$  NMR spectrum of  $3\text{-N}_2$  at 223 K but discrete coupling to  $^{31}\text{P}$  or  $^1\text{H}$  nuclei was not discerned.
- (17) Curiously, the presence of three  $^1\text{H}$  resonances (relative integral 6:3:3) observed upfield of  $\delta = 0$  ppm can be attributed to isopropyl C-H bonds that are engaged in agostic interactions with an Fe center (Figure 2). On warming to 293 K, the upfield isopropyl  $^1\text{H}$  resonances broaden and shift back to lower fields, concomitant with a coalescence of the hydride resonances into a single broad feature, suggesting that the agostic interactions are only observed at low temperatures in the absence of additional  $\text{N}_2$ .
- (18) Katayama, T.; Nitta, T. *J. Chem. Eng. Data* **1976**, *21*, 194.
- (19) Suess, D. L. M.; Tsay, C.; Peters, J. C. *J. Am. Chem. Soc.* **2012**, *134*, 14158.
- (20) Boncella, J. M.; Green, M. L. H.; Ohare, D. J. *Chem. Soc., Chem. Commun.* **1986**, 618.
- (21) Brown, S. D.; Mehn, M. P.; Peters, J. C. *J. Am. Chem. Soc.* **2005**, *127*, 13146.
- (22) Walter, M. D.; Grunenberg, J.; White, P. S. *Chem. Sci.* **2011**, *2*, 2120.
- (23) Pfirrmann, S.; Limberg, C.; Herwig, C.; Knispel, C.; Braun, B.; Bill, E.; Stosser, R. *J. Am. Chem. Soc.* **2010**, *132*, 13684.
- (24) Lowdin, P. O. *Phys. Rev.* **1955**, *97*, 1474.
- (25) Lubitz, W.; Reijerse, E.; van Gastel, M. *Chem. Rev.* **2007**, *107*, 4331.
- (26) Amara, P.; Mouesca, J. M.; Volbeda, A.; Fontecilla-Camps, J. C. *Inorg. Chem.* **2011**, *50*, 1868.
- (27) Harmer, J.; Finazzo, C.; Piskorski, R.; Ebner, S.; Duin, E. C.; Goenrich, M.; Thauer, R. K.; Reiher, M.; Schweiger, A.; Hinderberger, D.; Jaun, B. *J. Am. Chem. Soc.* **2008**, *130*, 10907.
- (28) Treatment of freshly prepared solutions of  $4\text{-(N}_2)_2$  with one equivalent of ferrocenium hexafluorophosphate in THF solution regenerates  $3\text{-N}_2$  in >90% yield ( $^1\text{H}$  NMR integration). While solid  $4\text{-(N}_2)_2$  is stable for extended periods,  $4\text{-(N}_2)_2$  decomposes in solution ( $t_{1/2}$  (298 K)  $\sim$  60 min). Repeating the ferrocenium oxidation on solutions of  $4\text{-(N}_2)_2$  after standing for 12 h does not recover  $3\text{-N}_2$  but instead furnishes a mixture of unidentified paramagnetic and diamagnetic species.
- (29) Münck, E. *Aspects of  $^{57}\text{Fe}$  Mössbauer Spectroscopy*; University Science Books: Sausalito, CA, 2000.
- (30) Robin, M. B.; Day, P. In *Advances in Inorganic Chemistry and Radiochemistry*; Emeléus, H. J., Sharpe, A. G., Eds.; Academic Press: New York, 1968; Vol. 10, p 247.
- (31) Allen, J. Bard, L. R. F. *Electrochemical Methods: Fundamentals and Applications*; 2nd ed.; John Wiley and Sons, Inc: New York, 2000.
- (32) Collman, J. P.; Brauman, J. I.; Iverson, B. L.; Sessler, J. L.; Morris, R. M.; Gibson, Q. H. *J. Am. Chem. Soc.* **1983**, *105*, 3052.
- (33) Yandulov, D. V.; Schrock, R. R. *Science* **2003**, *301*, 76.
- (34) Arashiba, K.; Miyake, Y.; Nishibayashi, Y. *Nature Chem.* **2011**, *3*, 120.
- (35) Hinnemann, B.; Norskov, J. K. *Top. Catal.* **2006**, *37*, 55.
- (36) Tondreau, A. M.; Stieber, S. C. E.; Milsman, C.; Lobkovsky, E.; Weyhermüller, T.; Semproni, S. P.; Chirik, P. J. *Inorg. Chem.* **2013**, *52*, 635.
- (37) Pickett, C. J.; Vincent, K. A.; Ibrahim, S. K.; Gormal, C. A.; Smith, B. E.; Best, S. P. *Chem.—Eur. J.* **2003**, *9*, 76.
- (38) Spatzal, T.; Aksoyoglu, M.; Zhang, L. M.; Andrade, S. L. A.; Schleicher, E.; Weber, S.; Rees, D. C.; Einsle, O. *Science* **2011**, *334*, 940.
- (39) Lancaster, K. M.; Roemelt, M.; Ettenhuber, P.; Hu, Y. L.; Ribbe, M. W.; Neese, F.; Bergmann, U.; DeBeer, S. *Science* **2011**, *334*, 974.
- (40) Lee, S. C.; Holm, R. H. *Chem. Rev.* **2004**, *104*, 1135.
- (41) Doan, P. E.; Telser, J.; Barney, B. M.; Igarashi, R. Y.; Dean, D. R.; Seefeldt, L. C.; Hoffman, B. M. *J. Am. Chem. Soc.* **2011**, *133*, 17329.
- (42) Zhang, J.; Gandelman, M.; Herrman, D.; Leitens, G.; Shimon, L. J. W.; Ben-David, Y.; Milstein, D. *Inorg. Chim. Acta* **2006**, *359*, 1955.
- (43) Rittle, J.; Peters, J. C. *Proc. Natl. Acad. Sci. U. S. A.* **2013**, *110*, 15898.
- (44) Bouwkamp, M. W.; Lobkovsky, E.; Chirik, P. J. *J. Am. Chem. Soc.* **2005**, *127*, 9660.
- (45) Chiang, K. P.; Bellows, S. M.; Brennessel, W. W.; Holland, P. L. *Chem. Sci.* **2014**, *5*, 267.
- (46) Thermodynamic measurements of  $\text{N}_2$  binding in synthetic systems invariably display large negative entropies. See ref 19 and references therein.
- (47) Wang, W. G.; Nilges, M. J.; Rauchfuss, T. B.; Stein, M. J. *Am. Chem. Soc.* **2013**, *135*, 3633.
- (48) Kinney, R. A.; Saouma, C. T.; Peters, J. C.; Hoffman, B. M. *J. Am. Chem. Soc.* **2012**, *134*, 12637.
- (49) Smith, J. M.; Lachicotte, R. J.; Holland, P. L. *J. Am. Chem. Soc.* **2003**, *125*, 15752.
- (50) Jablonskyte, A.; Wright, J. A.; Fairhurst, S. A.; Peck, J. N. T.; Ibrahim, S. K.; Oganessian, V. S.; Pickett, C. J. *J. Am. Chem. Soc.* **2011**, *133*, 18606.
- (51) Lukoyanov, D.; Yang, Z. Y.; Dean, D. R.; Seefeldt, L. C.; Hoffman, B. M. *J. Am. Chem. Soc.* **2010**, *132*, 2526.
- (52) Brookhart, M.; Grant, B.; Volpe, A. F. *Organometallics* **1992**, *11*, 3920.
- (53) Weitz, I. S.; Rabinovitz, M. *J. Chem. Soc., Perkin Trans. 1* **1993**, 117.
- (54) Barlow, S.; Murphy, V. J.; Evans, J. S. O.; Ohare, D. *Organometallics* **1995**, *14*, 3461.
- (55) Berto, T. C.; Hoffman, M. B.; Murata, Y.; Landenberger, K. B.; Alp, E. E.; Zhao, J. Y.; Lehnert, N. *J. Am. Chem. Soc.* **2011**, *133*, 16714.
- (56) Evans, D. F. *J. Chem. Soc.* **1959**, 2003.
- (57) Stoll, S.; Schweiger, A. *J. Magn. Reson.* **2006**, *178*, 42.
- (58) Weatherburn, M. W. *Anal. Chem.* **1967**, *39*, 971.